Research Square

Preprints are preliminary reports that have not undergone peer review.
They should not be considered conclusive, used to inform clinical practice,
or referenced by the media as validated information.

Failure-Diagnosis-Driven Spline Optimization Design for All-Terrain Vehicle Differential Gear Tooth Roots and a Dual-Objective Decision Framework

Haowei Li

195683318450163.com

Hebei Vocational University of Technology and Engineering https://orcid.org/0009-0009-8777-2102

Zexuan Jiao

Hebei Vocational University of Technology and Engineering

Shuaige Wang

Hebei Vocational University of Technology and Engineering

Pengcheng Sheng

Hebei Vocational University of Technology and Engineering

Ziming Wang

Hebei Vocational University of Technology and Engineering

Jinpu Zhang

Hebei Vocational University of Technology and Engineering

Yijia Shao

Hebei Vocational University of Technology and Engineering

Research Article

Keywords: Small all-terrain Vehicle, Differential Gears, Fault Diagnosis, Variable 36 Curvature Tooth Root, ANSYS, EMA Analysis

Posted Date: September 4th, 2026

DOI: https://doi.org/10.21203/rs.3.rs-10805017/v1

License: This work is licensed under a Creative Commons Attribution 4.0 International License.
Read Full License

Failure-Diagnosis-Driven Spline Optimization Design for All-Terrain Vehicle Differential Gear Tooth Roots and a Dual-Objective Decision Framework

Haowei Li[2], Zexuan Jiao[1,2*], ShuaigeWang[2],Pengcheng Sheng[1,2],ZimingWang[1,2],Jinpu Zhang[1,2], Yijia Shao[1,2]

[1]Hebei Special Vehicle Modification Center, Ltd., Xing'tai, China.

[2]Hebei Vocational University of Technology and Engineering, Xing'tai, China.

*** Correspondence:**

Zexuan Jiao

1031611165@qq.com

Abstract

Small all-terrain vehicles (ATVs) are widely used in complex off-road operations and competitive scenarios. Their transmission system gears are prone to fatigue fractures under the combined effects of impact loads and wide-band vibrations, which is a key bottleneck affecting vehicle reliability. This study addresses the issue of fractured differential axle gears during durability testing in a competition vehicle and establishes a systematic design framework of 'failure diagnosis—mechanism explanation—structural optimization—comprehensive verification.' Using finite element numerical simulation and precise path stress partitioning, the high-risk fracture areas were accurately pinpointed to the gear root's transverse [2.8, 4.2] mm and longitudinal [3, 5] mm ranges. Variable control analysis revealed how the stress direction angle at the gear root modulates peak stress, identifying 38° as the most unfavorable load angle with a peak stress of 680 MPa, a relative change of 16.9%. Experimental modal analysis (EMA) identified the first bending mode frequency of the gear as 3637.5 Hz, which overlaps with the main excitation frequency band of 1−5 kHz typical for ATV bumpy roads, creating a resonance amplification risk. Metallographic analysis confirmed that the failure mode was tooth surface pitting dominated by overload impacts, accompanied by anomalies in the carburized layer microstructure. To address these multiple failure causes, a variable-curvature gear root optimization scheme based on cubic B-splines was proposed, using its local support to precisely control the curvature in high-risk areas, smoothly increasing the root fillet radius from 0.5 mm to 1.5 mm. After optimization, the maximum equivalent stress at the gear root decreased from 688.95 MPa to 601.45 MPa (a reduction of 12.7%), and the first bending mode frequency increased from 3637.5 Hz to 4418.75 Hz (a rise of 21.5%), successfully avoiding the 15% resonance safety margin zone. On this basis, a continuous stress-curvature radius response model was established using Physics-Constrained Interpolation (PCI), and a dual-objective optimization envelope (BOE) decision framework was proposed. The BOE range satisfying static strength (90% gain) and dynamic stability (15% frequency margin) was defined as $R \in [1.32,1.60]$ mm, with a recommended engineering lower limit of $R \geq 1.40$ mm. The integrated diagnosis—optimization—verification method established in this study provides a reusable technical pathway and theoretical basis for fatigue-resistant design of gears in small ATV transmission systems.

Keywords: Small all-terrain Vehicle; Differential Gears; Fault Diagnosis; Variable Curvature Tooth Root; ANSYS; EMA Analysis

1 Introduction

Small all-terrain vehicles (ATVs) are widely used on complex unpaved surfaces, where driving conditions are highly unsteady (severe bumps, fluctuating traction coefficients, alternating load changes), which puts extremely high reliability demands on the transmission system. The differential gears, being key components for power transmission and differential coordination, experience severe root stress concentration and frequent fatigue fractures under the combined effects of impact loads and wide-frequency vibrations, and have become a technical bottleneck limiting lifespan improvement[1]. The off-road tracks of the China Baja Competition (BSC), including humps, washboard roads, mud, and rocks, realistically replicate extreme load spectra and are ideal test grounds for studying transmission failures. In 2025, a vehicle in the endurance race experienced gear idling after a differential abnormal noise. Upon disassembly, the axle gears were found to be severely worn and broken, with fractures near the gear root fillet, showing mixed overload and fatigue characteristics. Preliminary analysis suggested multiple coupled factors such as insufficient static strength, unfavorable load directions, dynamic resonance, and abnormal material structure[2]. Traditional optimization separately addresses static strength or dynamic characteristics and lacks systematic recognition and coordinated optimization of multiple causes. To address this, this study uses a range of systematic methods including finite element numerical simulation, precise path stress partitioning, control variable analysis, experimental modal analysis, and metallographic inspection. By comprehensively considering the coupling relationships between gear surface load spectra, stress angles, natural frequencies, and track excitation frequencies, the study performs static fracture analysis, spatial localization of high-risk areas, stress angle impact analysis, and dynamic resonance risk assessment[3]. Based on the results, the gears were redesigned, using variable-curvature splines to optimize the gear root structure. For small-sample data conditions, a physical-constraint interpolation dual-objective envelope (PCI-BOE) decision method was proposed, offering a reusable design paradigm for gear optimization with limited data. The optimization was ultimately validated, providing a theoretical basis for the design of the Baja racecar transmission system.

2 Analysis of Failed Gear Load and Risk Area Positioning

Due to a differential gear breaking during the car race, causing a failure to transmit power, the inspection after disassembly showed that the axle gears were severely worn, as shown in Figure 1. This study conducts an ANSYS finite element analysis on the axle gears, focusing on gear contact points and surfaces, the maximum fracture load, and the maximum deformation, along with other related fracture factors[4].



Figure 1 worn gear

2.1 Gear Equivalent Load Analysis

Finite element analysis requires applying a reasonable load on the gear surface. In this article, based on the whole vehicle parameters, as shown in Table 1, the input torque of the axle gear is determined from both the power source and ground adhesion aspects, and then the normal force acting on the gear surface is calculated.

Table 1 Vehicle and Gear Parameters

Parameters	Data
Motor output torque (T)	70N·M
Gearbox transmission ratio （i_a）	2.75
Differential transmission ratio （i_b）	2.58
Full load mass （i）	7.09
Full load mass （m）	220
Tire radius （r_a）	270
Road adhesion coefficient（μ）	0.5-0.6
Axle gear pitch circle radius（r_b）	21.25mm
Gear pressure angle（α）	20

(1) Determining the reference torque

Let the motor's peak output torque be T (N·m), and the total transmission ratio from the motor to the half-shaft be i (including the reducer and differential)

$$i = i_a \times i_b \tag{1}$$

Then the torque transmitted from the motor to the half-shaft is:

$$T_c = T \times i \tag{2}$$

After calculation, the torque transmitted from the motor to the half-shaft is 496.3 N·m. The maximum driving torque that the ground adhesion can handle is limited by the fully loaded mass of the race car m (kg), the tire radius r (m), and the road adhesion coefficient μ. Taking gravitational acceleration g, the torque limited by adhesion is:

$$T_t = \mu mg \cdot r \tag{3}$$

Among them, this is the torque limited by adhesion. In actual driving, the torque on the axle gear won't exceed the smaller of the two mentioned above. Calculations show that the reference torque is 320.2 N • m.

(2) Torque analysis under impact conditions

When the Baja car passes over the hump bump obstacle, the gears experience a significant impact load. Referring to the mechanical design manual and relevant studies on Baja cars, the impact factor is taken as 1.75[5]. Therefore, the torque used for finite element analysis is:

$$T_a = K_A \cdot T_t \tag{4}$$

(3) Calculation of the normal force on the tooth surface

According to calculations, 560.35 N·m, based on gear mechanics principles, the normal force on a single tooth surface is related to the torque, pitch circle radius, and pressure angle as follows:

$$F_n = \frac{T_a}{2r_b \cdot \cos\alpha} \tag{5}$$

This article treats this axial force as the equivalent load applied to a single gear tooth surface of the half-shaft gear, with the direction along the tooth surface normal. By inputting the calculated value of 1.135×10^4 N·M into the finite element model, the subsequent stress analysis can be carried out. For the material, the half-shaft gear is set as an isotropic standard elastic material, with a density of 7,850 kg/m³, an elastic modulus of 209 GPa, and a Poisson's ratio of 0.275. Hexahedral elements (C3D8R) and tetrahedral elements (C3D10M) are used for meshing. After consulting relevant references and balancing analysis error with accuracy, the local mesh size was finally set to 0.5 mm[6]. Considering all the factors from the calculations above, a contact stress of 1.135×10^4 N·M is applied to the gear surface.gear surface.



Figure 2 Overall Model Setup

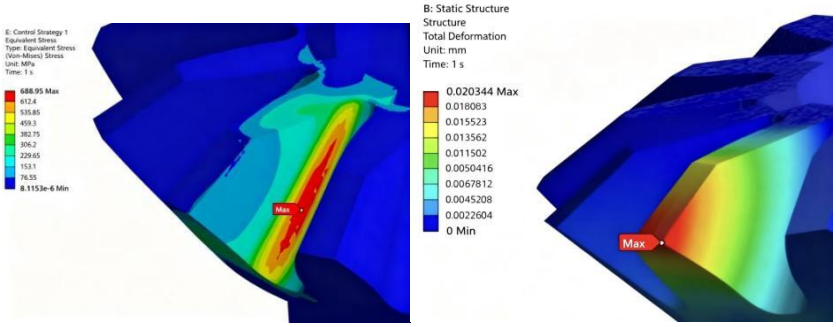


Figure 3 Gear Finite Element Analysis Model

As shown in Figure 2, a finite element analysis model of the differential axle gear was established. The analysis results show that the maximum equivalent stress of 688.95 MPa appears at the tooth root, and the maximum deformation of 0.020344 mm is located at the free end of the tooth top, gradually decreasing along the tooth height to the root. The finite element analysis results are shown in Figure 3.

2.2 Multi-interval Deformation Stress Analysis

Since the range of extreme stress is quite broad and the exact fracture location can't be pinpointed, we're considering using the SpaceClaim module to divide the geometry of the stressed surface. The gear tooth grooves are relatively intact without wear marks, so we're using the centerline of the grooves as the starting line to define paths for dividing the equivalent region of plane strain. Within this area, multiple horizontal and vertical paths are laid out at 1mm intervals based on the groove centerline and edge lines, as shown in Figure 4, with the perimeter area shown in Figure 5.

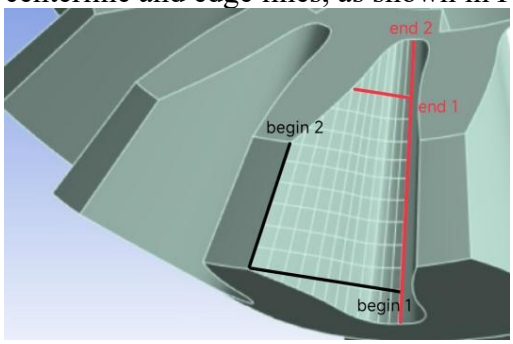


Figure 4 Horizontal and vertical path division

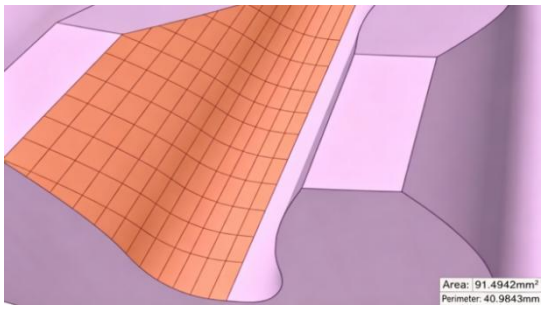


Figure 5 Path division, perimeter, area

Compare the maximum stress values along different longitudinal paths, using the midpoint of the tooth slot as a reference, and extract data at 1mm intervals, getting about 10 data samples. From these,

divide them into 3 groups of highly accurate and representative data to serve as the final experimental data samples. Part of the data for the longitudinal distribution curve of equivalent stress is shown in Figure 5.

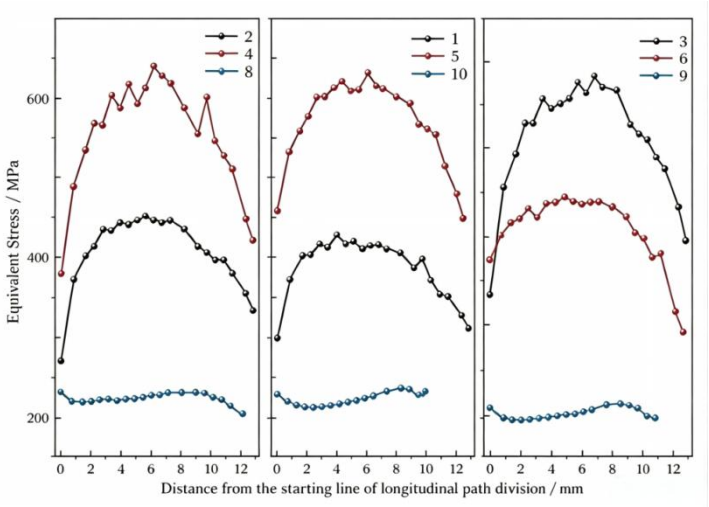


Figure 6 Full Longitudinal Section

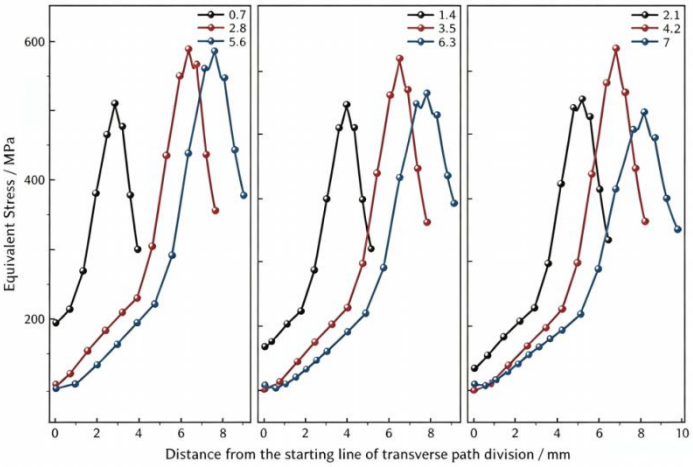


Figure 7 full horizontal section

Based on the analysis of the full longitudinal section in Figure 6:

The longitudinal path stress extraction results are shown in Figure 6. The stress along the length of the tooth slot is unevenly distributed, with a peak stress of 679.83 MPa appearing 4 mm from the centerline of the slot. The numerical deviation from the maximum value in the overall finite element analysis is within 1.3%, which verifies the consistency of the model accuracy. High-risk areas are concentrated within the longitudinal range of [3, 5] mm. Multiple stress distribution lines overlap in this region, and after rising rapidly, the stress tends to stabilize, with overall fluctuations of about 15%. This is a key area for tooth root fracture. Further comparison of the maximum stress values along different transverse paths, with data extracted using intervals based on a 0.7 mm distance from the edge of the tooth slot, yields the equivalent stress transverse path distribution curve shown in Figure 7.

Based on the analysis of the full transverse section in Figure 7:

The transverse path stress extraction results are shown in Figure 6. The stress shows a clear inverted parabolic trend, reaching a peak of 688.95 MPa at 4.2 mm from the edge of the tooth slot. High-risk

areas are concentrated within the transverse range of [2.8, 4.2] mm, where extreme points are densely distributed and all exceed 600 MPa. The transverse high-risk area is precisely located within 2.8 – 4.2 mm from the centerline of the slot.

Combining the longitudinal and transverse path analysis results, the high-risk area for gear fracture is accurately located in a local part of the tooth slot—transversely [2.8, 4.2] mm and longitudinally [3, 5] mm. This positioning provides a precise spatial basis for subsequent control variable analysis of high-risk areas.

3 Analysis of Multi-Variable Load Effects in High-Stress Areas

3.1 Analysis Plan Design

We analyzed and pinpointed the high-risk transverse fracture zone in the gear structure at [2.8, 4.2] mm and the longitudinal zone at [3, 5] mm. Based on this data, to further study how stress values and stress angles affect fractures in these high-risk gear areas, a controlled variable analysis approach was used. Using the equivalent area of the high-risk zone (91.48 mm²) obtained from the path segmentation in Chapter 1 and the average stress level in that area, we calculated the reference value for the maximum principal stress in the high-risk zone to be 124.6 MPa. This serves as the fixed stress value for the controlled variable analysis. By keeping the stress value constant and changing the stress angle, we carried out the controlled experiments. Reviewing relevant studies shows that the direction of the maximum principal stress forms about a 35°~55° angle with the normal of the tooth root surface[7], and this angle changes with the load application point. At the upper boundary of a single tooth pair engagement, the direction of the maximum principal stress at the tooth root is typically around 43°, and it shifts as the load moves across the tooth surface[8].

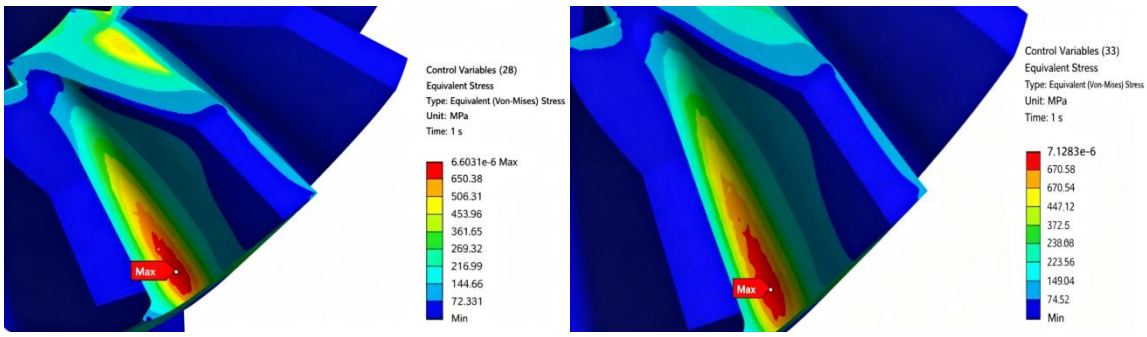
With all this in mind, we conducted controlled variable experiments: based on the high-risk zone precisely located in Section 2.2 (transverse [2.8, 4.2] mm, longitudinal [3, 5] mm), we designed multiple sets of controlled variable experiments:

3.2 Controlled variable analysis experiment

The controlled variable experiment is mainly divided into 5 groups, controlling fixed stress values and varying stress angles, as shown in Table 2.

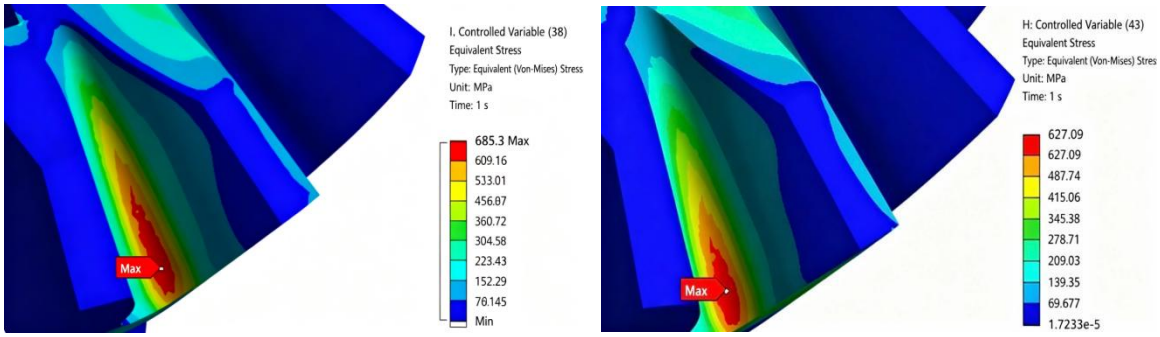
Table 2: Control Variable Experimental Design

Experimental Group	Control Method	Fixed Parameters	Experimental Purpose	Variable Parameters
Group 5	Fixed stress value, changing stress angle	Maximum principal stress value is 124.6 NM	To study the effect of stress direction on local stress concentration areas at the tooth root and fracture patterns	Stress angle parameter gradient: 28°, 33°, 38°, 43°, 48°



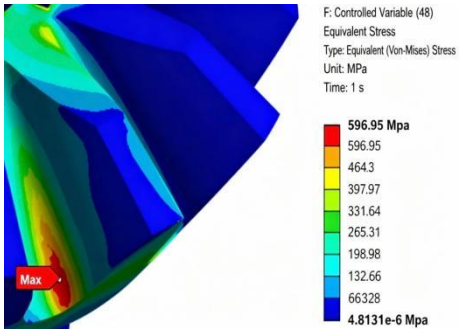
186

187 Figure 8 28°,33° Stress Diagram



188

189 Figure 9 38°,43°Stress Diagram



190

191 Figure 10 48°Stress Diagram

192 According to the precise path division in Section 1.2, the effective surface area of the action path is
193 91.48 mm², and the maximum principal stress in the fixed high-risk area is 124.6 MPa. A stress
194 direction angle analysis was carried out in the range of 28° to 48° with 5° increments. As shown in
195 Figures 8-10, by comparing the equivalent stress cloud diagrams for each angle, we can see that in
196 the 28° to 38° range, the peak equivalent stress gradually rises from 650 MPa to 680 MPa as the
197 angle increases. The mechanical reason is that the tangential load component increases with the angle,
198 making the tooth root bending tensile stress increasingly dominant and intensifying stress
199 concentration. When the angle reaches 38°, the tangential bending tensile stress and the normal
200 contact compressive stress form an optimal coupling at the high-risk section, producing the strongest
201 superposition effect, with the peak stress reaching 680 MPa. If the angle continues to increase to 48°,
202 the peak stress drops to 570 MPa, a decrease of 16.2%, because the normal load component gradually
203 misaligns with the tooth root fillet normal direction, weakening the superposition effect of tangential
204 and normal stresses, and the force flow reroutes along the tooth surface, easing local stress
205 concentration.

This analysis shows that within the 20° range of 28° to 48°, the peak stress difference reaches 110 MPa, with a relative change of 16.9%, which is significant. Thus, 38° is determined to be the most unfavorable load direction angle for this gear structure.

4 Comprehensive verification of failure mechanisms

In Chapter 2, finite element analysis precisely pinpointed the high-risk fracture area to the [2.8, 4.2] mm range laterally and [3, 5] mm range longitudinally at the tooth root. Chapter 3 further identified 38° as the most unfavorable load direction. However, stress analysis only reveals the mechanical driving factors behind the fracture, so we still need to cross-verify the failure mechanism from the perspectives of material microstructure and structural dynamic properties. To do this, this chapter carries out metallographic analysis (Section 4.1) and experimental modal analysis (Section 4.2), checking the consistency of the conclusions from Chapters 2 and 3 at both the micro material strength and macro vibration response levels, and revealing the fracture mechanism under the combined effect of static stress concentration and dynamic load resonance amplification.

4.1 Metallography

To further clarify the cause of the gear fracture and evaluate the metallurgical quality of the raw materials and the reasonableness of the heat treatment process, a systematic metallographic analysis was carried out on the failed gear. The sampling locations are shown in Figure 11, including the fracture debris inside the differential housing and the gear tooth contact area. After mounting, grinding, and polishing, the microstructure was observed using a scanning electron microscope (SEM) [9].



Figure 11: Sampling of metallographic test specimens

Based on the metallographic analysis of the phases at 200x and 500x magnification (Figure 12), the following can be observed:

From the morphology (dense gray-black matrix + diffused fine dark particles):

1. Matrix: Fine tempered martensite (high carbon, carburized surface structure)

After carburizing, the surface carbon content increases. Quenching and low-temperature tempering form fine needle-like/cryptocrystalline tempered martensite, which is the main body for wear resistance of the gear tooth surface (tooth surface hardness HRC58~63);

2. Diffuse small black particles: Granular alloy carbides + trace amounts of retained austenite

Fine particles: Cr alloy carbides precipitated during the carburizing process (improving wear resistance and pitting resistance); Light white diffused area: Quenched retained austenite (normal associated structure in carburized gears);

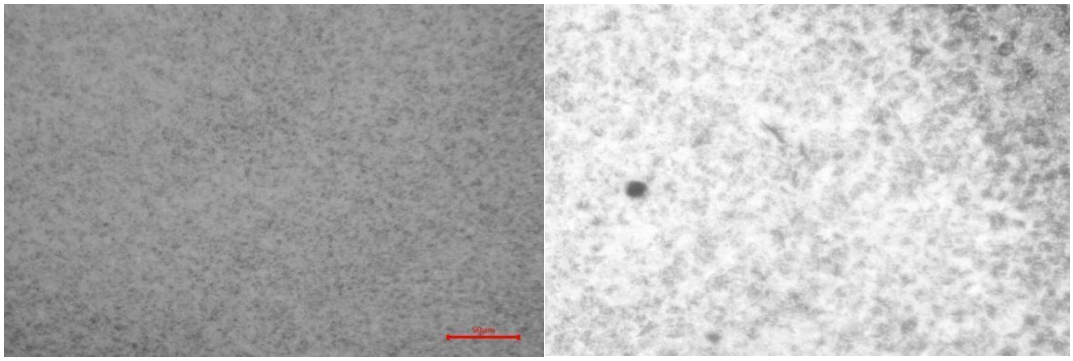


Figure 12 Metallographic Structure (200x, 500x)

Metallographic observation confirmed that the fracture surface was characterized by surface spalling dominated by overload impact, accompanied by localized carbide segregation and a high content of retained austenite in the carburized layer. These microstructural features reduced the surface impact toughness to some extent, accelerating wear and chipping. The spatial location of this spalling feature closely matches the high-stress zone (transverse [2.8, 4.2] mm, longitudinal [3, 5] mm) identified in Chapter 2, which is precisely the stress concentration zone under the 38° critical load direction determined in Chapter 3. These three findings corroborate each other, indicating that the fracture was caused by stress concentration in the high-risk area exceeding the material's microstructural strength limit under a specific load direction.

4.2 Experimental modal analysis

Metallographic analysis revealed the failure mechanism under static overload conditions but failed to explain why fractures occurred concentratedly under specific working conditions. The Baja all-terrain vehicle exhibits short-duration high-impact and broadband random vibration characteristics during operation. Therefore, this study further investigated resonance risks from a dynamic characteristics perspective using Experimental Modal Analysis (EMA). Based on the Engineering Data Management (EDM) software platform, its EMA modal analysis module was used for hammer impact testing and data acquisition. The EDM platform then employed modal analysis to optimize the system's dynamic characteristics.

4.2.1 EDM Platform Setup

Connect the DSS device (testing instrument) and set the excitation level of the excitation sensor hammer to 10V and the sensitivity to 98.88 to generate detailed images. A triaxial accelerometer capable of simultaneously measuring vibration acceleration signals in the X, Y, and Z directions is fixed to the gear as shown in Figure 13. The experimental gear is fixed to the stand, and the trigger type, analysis frequency, block size (line/block), window type, and superposition rate are set as shown in Table 3. A hammer impact test is performed.



Figure 13 Experimental gear fabrication

Table 3 Trigger Type Parameters

Analysis Frequency (Hz)	3.5kHz
Block Size (lines/block)	1024/450
Window Type	Uniform
Overlay Rate	No Overlay
Averaging Mode	Linear
Average	4

4.2.2 High and low frequency modes

As shown in Figure 14, the low-frequency modal curves show a significant peak at approximately 3637.5 Hz, with an amplitude of approximately -43.69 dB on a logarithmic scale of 0.0113 g/N. Simultaneously, the phase frequency curve undergoes a sudden change of approximately -180° near this frequency. These characteristics are consistent with the typical manifestations of system resonance: amplitude peak, phase crossing of -90°~-270° or -180° sudden change [10]. Therefore, 3637.5 Hz is determined to be the first-order bending mode or local resonance frequency of the gear system. This frequency is located on the typical bumpy surface of the Baja racetrack, which contains high-frequency impact components of 1~5 kHz [11]. When the original race car passed through the hump obstacle, the broadband random excitation from the road surface excited this mode, resulting in a significant amplification of the dynamic stress at the root of the gear teeth, thereby accelerating the initiation and propagation of fatigue cracks. This inference is highly consistent with the location of the maximum equivalent stress zone at the tooth root in the finite element analysis in Section 1, which is [2.8, 4.2] mm laterally and [3, 5] mm longitudinally, further confirming that dynamic resonance is an important cause of fracture.

As shown in Figure 15, the high-frequency modal curves also show a clear amplitude peak at 8782.50 Hz. The amplitude at 5.3878 g/N is significantly -17.41 dB on the logarithmic coordinate, and the phase also shows a change of about -130°, indicating that this frequency corresponds to the higher-order bending mode or the local vibration mode of the tooth surface [12]. The peak amplitude at 8782.50 Hz is relatively low and the bandwidth is narrow, which is likely due to the secondary resonance of the hammer or the higher-order mode of the test fixture. It has limited impact on the actual working conditions and can be temporarily disregarded in subsequent optimization.

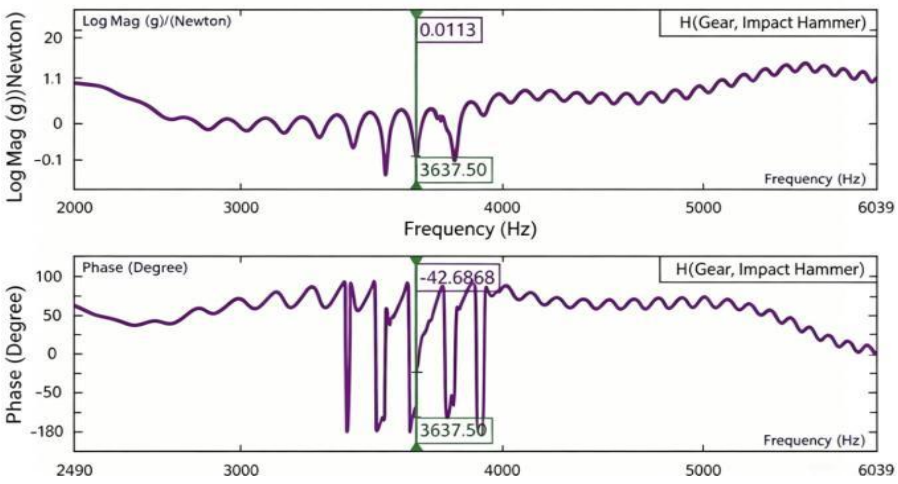


Figure 14 Amplitude-frequency characteristic curves of FRF low-frequency band modes

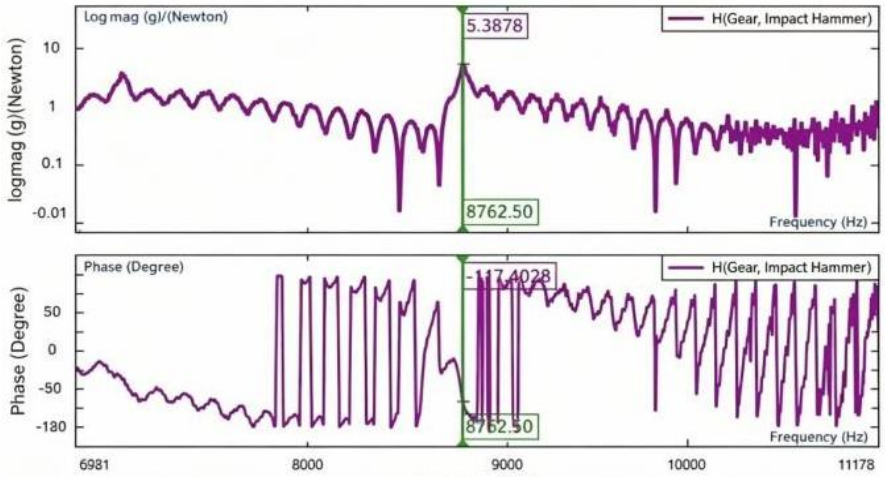


Figure 15. Amplitude-frequency characteristic curves of FRF high-frequency band modes

4.3 Comprehensive determination of failure mechanism

The combined results of metallographic analysis and experimental modal analysis indicate that the wear fracture primarily occurs at the static and dynamic levels:

Statically: Stress concentration in the high-risk area (688.95 MPa) coupled with the most unfavorable load direction (38°) causes the local stress at the tooth root to exceed the material's microstructural strength limit, creating the mechanical conditions for crack initiation;

Dynamically: The first-order bending mode frequency (3637.5 Hz) falls into the main excitation frequency band of the track, dynamically resonating and amplifying the stress amplitude at the tooth root, accelerating crack propagation;

The synergistic effect of these two factors leads to the early fracture failure of the gear under durability conditions.

5 Tooth root optimization and PCI-BOE decision method based on variable curvature splines

Finite element analysis shows that the maximum equivalent stress at the tooth root in the original design reaches 688.95 MPa, with the high-risk area concentrated in the narrow local zone of the tooth root transition arc. To fundamentally reduce the stress concentration level at the tooth root, this chapter establishes mathematical models for both traditional circular arc tooth roots and variable curvature spline tooth roots based on parametric modeling theory. The fatigue-resistant design of the tooth root structure is achieved through curvature distribution optimization[13].

5.1 Traditional circular arc tooth root mathematical model

In the tooth root transition region, a local coordinate system is established with its origin at the intersection of the tooth groove centerline and the tooth root circle. The x-axis is along the tooth groove centerline, and the y-axis is along the tooth width direction. The geometric equation of the traditional circular arc tooth root can be expressed as:

$$x^2 + \left(y - y_c\right)^2 = R_0^2 \left(y \le y_c\right) \tag{6}$$

The resulting stress concentration factor Kt can be approximately expressed using the Neuber formula or the Peterson formula as follows:

$$K_t = 1 + \frac{2}{R_0}\sqrt{\frac{a}{\rho_{eff}}} \tag{7}$$

K_t —Theoretical stress concentration factor $K_t = \dfrac{\sigma_{\max}}{\sigma_{nom}}$

a —Gap depth

ρ_{eff} —Equivalent radius of curvature at the root of the notch

$\sigma_{\max}$ —Actual peak stress

σ_{nom} —nominal stress

For a circular arc with constant curvature as shown in Figure 16, K_t maintains a constant maximum value throughout the entire tooth root segment, resulting in stress concentration that cannot be alleviated by local adaptation of the geometry. In the original design of this study, $R_0 = 0.5mm$, and the nominal stress $\sigma_{\text{nom}} = 550Mpa$ obtained from the finite element analysis, the actual peak stress at the tooth root $\sigma_{\max} = K_t \cdot \sigma_{nom} = 688.95Mpa$, which is consistent with the analysis in Section 2.1.

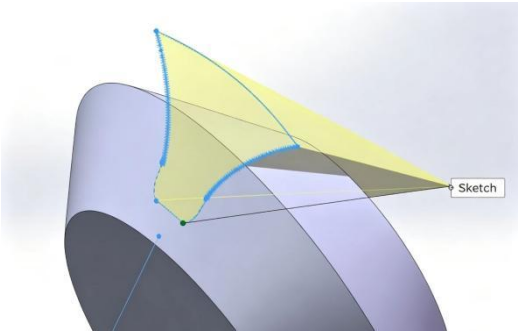


Figure 16 Traditional circular arc tooth root curve

5.2 Mathematical model of tooth root with variable curvature spline

For the tooth root transition curve, curvature continuity directly affects the transmission path of force flow across the tooth surface. Cubic B-splines offer a balance between curve smoothness and computational efficiency; quadratic splines cannot guarantee C2 curvature continuity, whereas splines of degree four or higher involve an excessively large influence range for control points, making localized adjustments in high-risk areas difficult. Therefore, this study employs cubic B-splines to construct the tooth root transition profile, with the following parametric equation:

$$C(t)=\sum_{i=0}^{n}N_{i,p}(t)\cdot P_i \tag{8}$$

In the equation, $C(t) = [x(t), y(t)]^T$ is the position vector on the curve at parameter t, n = 5 (indicating 6 control points), p = 3 is the spline degree, P_i represents the coordinates of the i-th control point, and $N_{i,p}$ (t) is the p-th degree B-spline basis function determined by the Cox-de Boor recurrence formula: the B-spline basis functions are determined by the following recurrence formula:

$$N_{i,0}(t)=\begin{cases}1\left(t_i\le t<t_{i+1}\right)\\0\left(otherwise\right)\end{cases} \tag{9}$$

$$N_{i,p}(t)=\frac{t-t_i}{t_{i+p}-t_i}N_{i,p-1}(t)+\frac{t_{i+p+1}-t}{t_{i+p+1}-t_{i+1}}N_{i+1,p-1}(t) \tag{10}$$

To ensure a smooth transition between the root curve and the straight section of the tooth profile, and the bottom of the tooth groove at the connection point, the following must be met:

$$C_{con}^{1}:\ C'(t_{1\text{ink}})=\lambda\cdot V_{\tan} \tag{11}$$

$$C_{con}^{2}:\ C''(t_{1\text{ink}})=\mu\cdot V_{\text{nor}} \tag{12}$$

Here, λ and μ are proportionality coefficients, while V_tangential and V_normal represent the tangential and normal vectors at the connecting boundary, respectively. Research by Vaghela and Prajapati indicates that the G^2 continuity constraint is the key geometric condition for eliminating stress concentration at the root junction [14]. The radius of curvature ρ(t) of the B-spline curve is given by:

$$\rho(t)=\frac{\left|C'(t)\right|^3}{\left|C'(t)\times C''(t)\right|} \tag{13}$$

$C'(t_{1\text{ink}})$ —First derivative of the curve at the connection point

$C''(t_{1\text{ink}})$ —Second derivative of the curve at the connection point

λ —Tangential continuity scaling factor

μ —Normal continuity scaling factor

$V_{\tan}$ —Tangent vector of the adjacent geometric feature

V_{nor} —Normal vector of the adjacent geometric feature

In the formula, C'(t)and C''(t)represent the first and second derivatives of the curve, respectively. A smaller ρ(t) indicates sharper curvature at the tooth root and more severe stress concentration, whereas a larger ρ(t)implies a gentler curve and alleviated stress concentration; by adjusting the positions of the control points,ρ(t) is made to transition continuously from $R_0 = 0.5\text{mm}$ to $R_{\max} = 1.5\text{mm}$ [15].As shown in Figure 17.

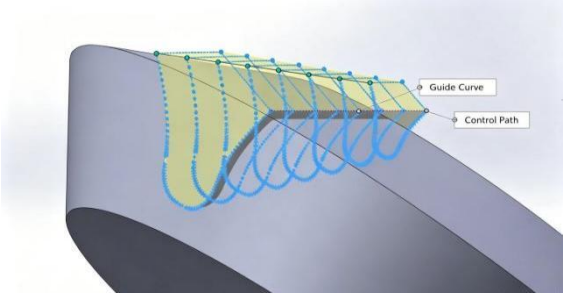


Figure 17 Variable-curvature spline tooth root curve

A key advantage of B-spline curves is their local support property: adjusting any single control point Pi affects the curve shape only within the parameter interval $t \in [ti, ti + p + 1]$, leaving the rest of the curve unchanged. This characteristic allows for localized, refined adjustments in high-risk zones (transverse range [2.8, 4.2] mm, longitudinal range [3, 5] mm) without the need to redesign the entire tooth root curve [16, 17]. The sequence of optimal control point coordinates {Pi} derived from the mathematical model is imported into SolidWorks; 6 to 8 control points are defined on the tooth root cross-section sketch to generate the transition curve. Fine-tuning the control points near the high-risk zone ensures a smooth transition of the radius of curvature from 0.5 mm to 1.5 mm, followed by a sweep operation along a 3D guide curve to complete the optimization of the tooth root surface . After optimization, the three intermediate control points (P1, P2, P3) are shifted outward by approximately 0.2 – 0.4 mm, resulting in a continuous transition of the tooth root radius of curvature from R0 = 0.5 mm to 1.5 mm.As shown in Figure 18.

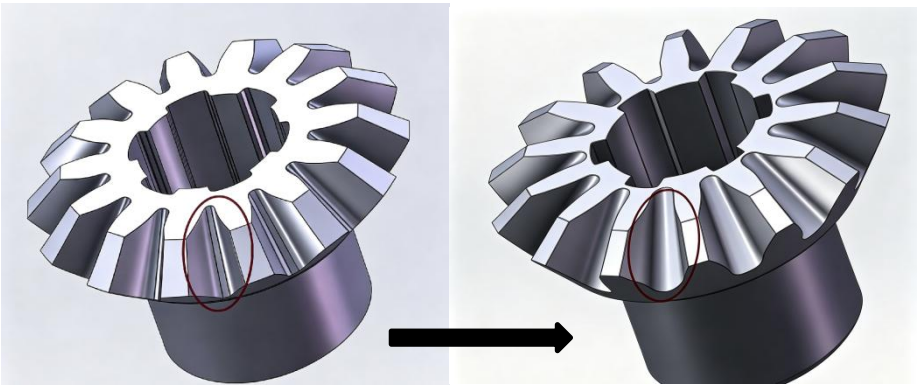


Figure 18 Modeling Optimization

5.3 Decision-making method for gear root optimization based on physics-constrained interpolation and dual-objective envelopes

Sections 5.1 and 5.2 established the geometric models for variable-curvature spline root fillets and determined the stress and frequency responses for two extreme design cases (R = 0.5 mm and R = 1.5 mm) via finite element analysis. However, engineering optimization requires not only verifying the feasibility of individual designs but also defining recommended parameter ranges based on limited data. To address this common challenge, this section proposes a structural optimization decision-making framework suitable for small datasets; the framework comprises two core components:

(1) Physics-Constrained Interpolation (PCI)—constructing a complete response curve by using the power-law relationship derived from classical stress concentration theory as a constraint and the two extreme data points as anchors [18];

According to the theory of stress concentration at the tooth root, a power-law relationship exists between the maximum root stress (σ) and the fillet radius (R).

$$\sigma(\mathrm{R}) = \alpha \bullet R^{-\mathrm{m}} + b \tag{14}$$

The exponent m is related to the tooth profile geometry; literature indicates that it falls within the range m $\in$ [0.3, 0.5][19]. In this study, m is set to 0.35 (a typical value for standard involute gears), and the coefficients a and b are determined using two finite element data points (R = 0.5 mm, σ = 688.95 MPa; R = 1.5 mm, σ = 601.45 MPa), yielding the following PCI model:

$$\sigma(\mathrm{R}) = 215.06 \times \mathrm{R}^{-0.35} + 414.84 \ \ (\mathrm{MPa}) \tag{15}$$

The fundamental distinction of the PCI method from traditional polynomial regression lies in the fact that the curve's shape is determined by physical laws rather than statistical fitting; consequently, it yields physically consistent predictions even with small sample sizes.

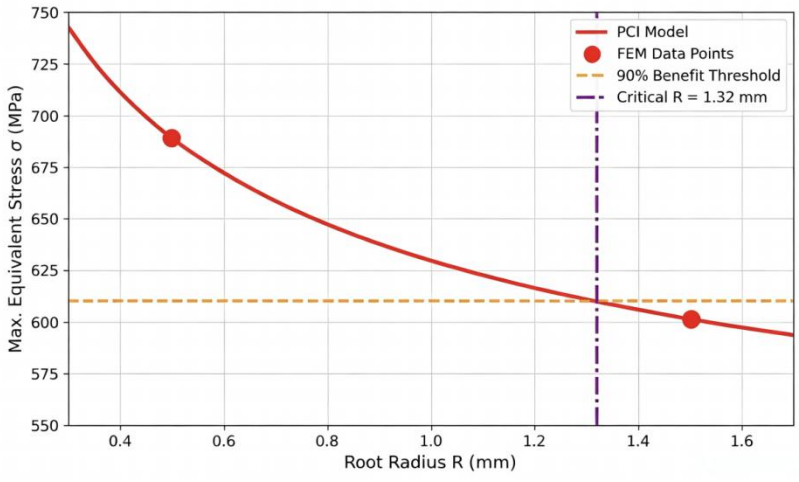


Figure 19 Comparison of the PCI model fitting curve with finite element data

Figure 19 illustrates the comparison between the PCI fitted curve and the original finite element data points. The red curve represents the relationship between root stress and radius of curvature predicted by the PCI model; the red dots indicate the finite element data points; the orange dashed line marks the 90% benefit threshold (610.20 MPa); and the purple dash-dotted line indicates the critical radius (1.32 mm). The model curve passes precisely through two data points, validating the effectiveness of

the fitted parameters (a=215.06, b=414.84) in accurately reflecting the data characteristics. The figure also displays the 90% benefit threshold line ($\sigma 90\% = 610.20$ MPa) and its corresponding critical radius ($R\sigma = 1.32$ mm).

Furthermore, to reveal the intrinsic relationship between the two optimization objectives—static strength and dynamic stability—Figure 20 plots the Pareto front extending from the initial design to the optimized point, with stress on the horizontal axis and frequency on the vertical axis. The front exhibits a monotonically decreasing trend, indicating that the two objectives do not conflict within the parameter range investigated in this study; specifically, a reduction in stress is accompanied by an increase in frequency, demonstrating a synergistic relationship between them[20].

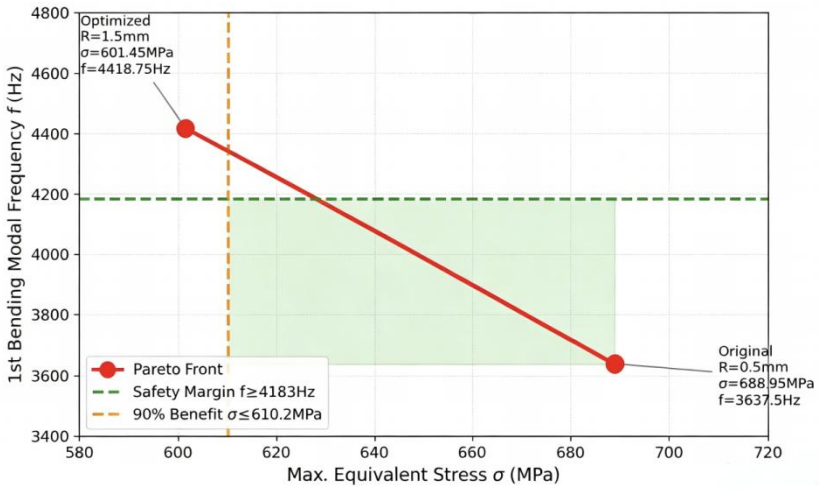


Figure 20 Dual-objective Pareto front and constraint boundary.

The solid red line represents the Pareto front extending from the initial design (R = 0.5 mm) to the optimized point (R = 1.5 mm); the orange dashed line indicates the 90% gain threshold ($\sigma \leqslant 610.20$ MPa), and the green dashed line marks the 15% frequency safety margin ($f \geqslant 4183$ Hz). The green shaded area represents the region where both objective constraints are simultaneously satisfied. The Pareto front exhibits a monotonically decreasing trend, indicating synergy between the two objectives rather than conflict.

(2) Bi-objective Optimization Envelope (BOE) — defined by constraints on static strength and dynamic stability, this envelope delineates the parameter range that simultaneously meets all performance requirements. The optimization problem is formulated as determining the feasible parameter region subject to these dual-objective constraints.

Static strength objective: A 90% gain cutoff criterion is defined — when changes in geometric parameters yield more than 90% of the total gain, the parameter enters the "optimal solution range." The total gain is $\Delta = 688.95 - 601.45 = 87.50$, and the stress threshold corresponding to 90% gain is $\sigma 90\% = 610.20$ MPa. Substituting this into Equation (15) and solving inversely yields:

$$R_{\sigma} \geq 1.32mm \tag{16}$$

To intuitively describe how the optimized gain varies with the radius of curvature, the gain ratio is defined as the percentage of the total stress reduction represented by the current stress reduction:

$$\text{Benefit}(R) = \frac{\sigma(0.5)-\sigma(R)}{\sigma(0.5)-\sigma(1.5)} \times 100\% \tag{17}$$

Figures 21 illustrate the variation of the gain ratio with the radius of curvature R. The curve exhibits a monotonically increasing trend; the gain rises rapidly within the range of R = 0.5–1.0 mm but

subsequently slows down, demonstrating characteristics of diminishing marginal returns. The intersection of the 90% gain threshold line and the gain curve occurs at R = 1.32 mm, which is consistent with the result calculated using Equation (15).

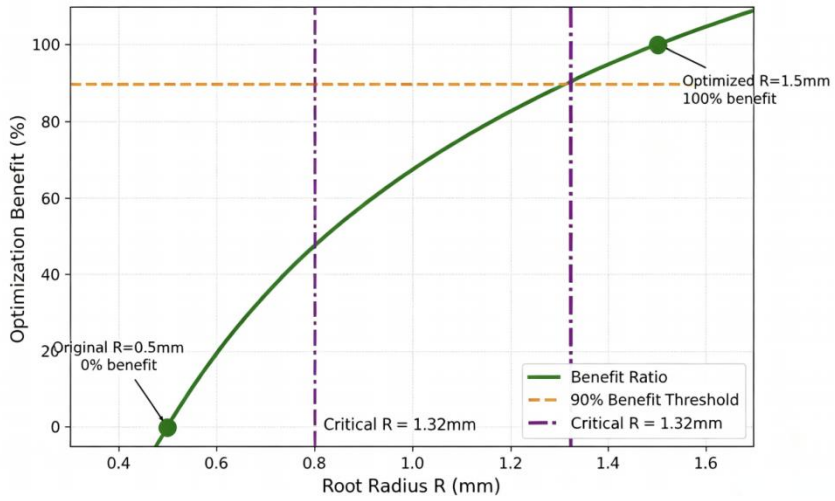


Figure 21 Optimized gain-to-curvature radius ratio curve

The green curve represents the variation of the optimized benefit ratio with the radius of curvature; the orange dashed line indicates the 90% benefit threshold, and the purple dash-dot line marks the critical radius (1.32 mm). The benefit curve rises rapidly in the R=0.5-1.0 mm range but subsequently levels off, exhibiting the law of diminishing returns. Considering computational accuracy and engineering safety margins, it is recommended to round the value to R $\geqslant$ 1.40 mm as the lower limit for engineering applications. Dynamic stability objective: Based on the EMA results from Chapter 4, the gear's first-order bending mode frequency must avoid the 15% resonance safety margin range—specifically, f $\geqslant$ 4183 Hz. The linear relationship between frequency and the radius of curvature is determined by two data points (R = 0.5 mm, f = 3637.5 Hz; R = 1.5 mm, f = 4418.75 Hz); solving this yields:

$$R_f \geq 1.20mm \tag{18}$$

Taking the intersection of the two yields the bi-objective optimization envelope (BOE):

$$R \in [1.32,1.60]mm \tag{19}$$

For engineering purposes, a value of R $\geqslant$ 1.40 mm is recommended; this value captures over 90% of the potential gains from static strength optimization while balancing dynamic stability requirements and manufacturing feasibility. The decision diagram based on the PCI-BOE framework is shown in Figure 22.

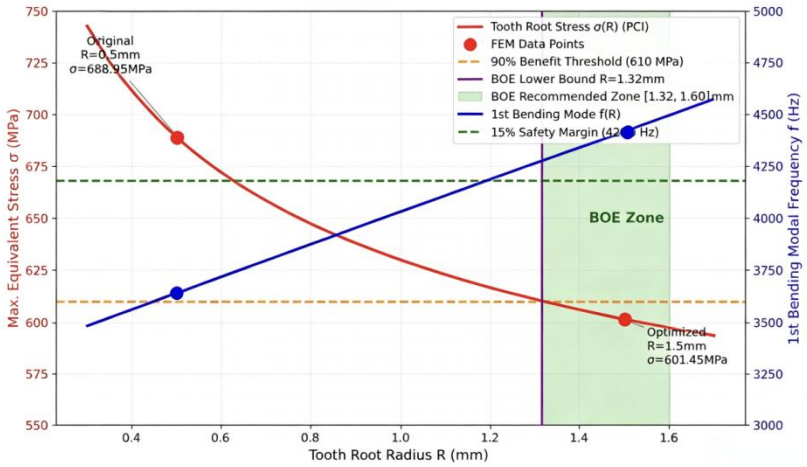


Figure 22 Bi-objective Optimization Envelope (BOE) Decision Diagram

The green shaded area represents the BOE (Best Operating Envelope) region; its left boundary (R = 1.32 mm) is determined by the theoretical value derived from static strength constraints, while the right boundary (R = 1.60 mm) is an engineering upper limit established by considering both geometric interference and the effect of diminishing marginal returns. For engineering applications, it is recommended to set the curvature radius to R ≥ 1.40 mm. The figure clearly demonstrates that: (1) when R < 1.32 mm, the tooth root stress exceeds the 90% benefit threshold, resulting in insufficient gains from static strength optimization; (2) when R ≥ 1.20 mm, the modal frequency already meets the 15% safety margin requirement, meaning this constraint does not play a dominant role within the BOE; and (3) within the BOE range (R = 1.32–1.60 mm), both objectives are satisfied, and the stress levels approach the optimal range. Given that the theoretical value of R = 1.32 mm is derived from an exact inverse solution based on the PCI model, and accounting for engineering uncertainties—such as finite element calculation errors, material property variations, and manufacturing tolerances—this paper recommends a lower limit of R ≥ 1.40 mm for practical application. This value captures over 90% of the potential static strength optimization benefits while maintaining sufficient margins for dynamic stability requirements and manufacturing feasibility. Figure 23 presents a normalized comparison of tooth root stress and the first-order bending modal frequency—using the original design (R = 0.5 mm) as the baseline (100%)—to comprehensively evaluate the overall static and dynamic improvements achieved by the optimization scheme.

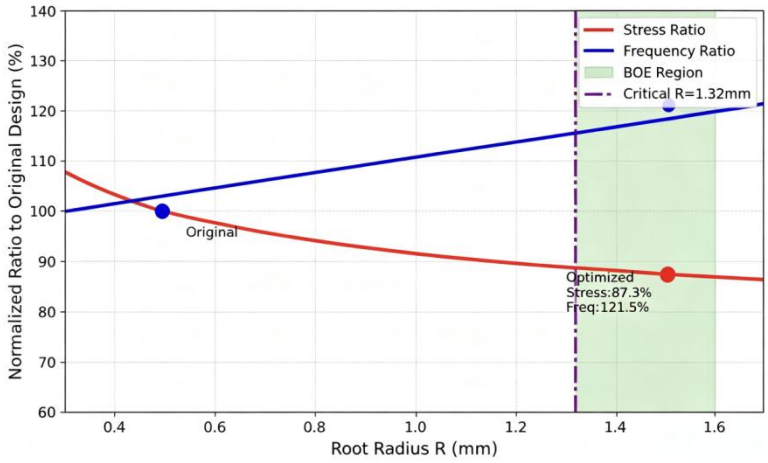


Figure 23 Normalized comprehensive comparison of static and dynamic characteristics

The red curve represents the stress ratio (normalized against the original design value of 688.95 MPa), the blue curve represents the frequency ratio (normalized against the original design value of 3637.5 Hz), the green shaded area indicates the BOE range (1.32–1.60 mm), and the purple dash-dotted line marks the critical radius. At R = 1.5 mm, the stress drops to 87.3% of the original design value while the frequency rises to 121.5%, achieving a simultaneous improvement in both static strength and dynamic stability.

Synthesizing the analysis results from Figures 19 through 23, the PCI-BOE decision-making framework proposed in this paper successfully identified the optimization parameter range satisfying dual-objective constraints—using only two finite element data points—and provided a clear engineering recommendation (R ≥ 1.40 mm). This framework does not rely on extensive parameter sweep data; it is characterized by high data efficiency, strong physical interpretability, and good generalizability, making it applicable to other structural optimization problems facing similar "data scarcity" conditions, such as gear root parameter design involving different modules, material properties, or loading conditions.

5.4 Experimental verification of the optimization scheme

To verify the practical effectiveness of the variable-curvature spline root optimization scheme presented in Section 5.2, this section employs the same load boundary conditions and testing parameters as the original design (as shown in Figure 24). Comprehensive evaluations of the optimized gear's static strength and dynamic stability are conducted using finite element static analysis and experimental modal testing, respectively.

Static analysis verification: The optimized 3D model (R = 1.5 mm) was re-imported into Ansys Workbench. Upon applying the same normal force (1.135×10^4 N) and impact factor ($K_A = 1.75$), the calculated maximum equivalent stress at the tooth root was 601.45 MPa—a 12.7% reduction compared to the original design (688.95 MPa), as shown in Figure 25. The peak stress location shifted approximately 0.6 mm from the midpoint of the tooth root arc toward the center-line of the tooth space; this indicates that the variable-curvature design transformed the stress concentration from a "point" into a "short band" distribution, resulting in a more gradual stress gradient. This stress value falls below the 90% benefit threshold (610.20 MPa) derived from the PCI model in Section 5.3, representing a static strength optimization benefit of 91.6%.



Figure 24 Construction of the optimized finite element model.

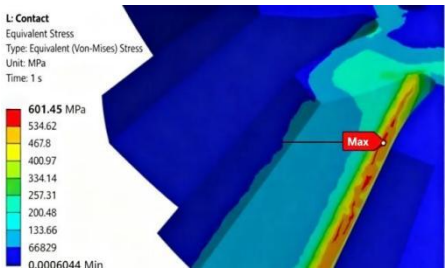


Figure 25 Finite element analysis of equivalent stress after optimization.

Dynamic verification: Based on impact testing using the EDM platform, the first-order bending mode frequency of the optimized gear in the low-frequency range increased from the original design's 3637.5 Hz to 4418.75 Hz—a rise of 21.5%. This frequency exceeds the lower limit of the 15% resonance safety margin (4183 Hz), successfully moving outside the track's primary excitation frequency band of 1–5 kHz (as shown in Figure26). Regarding the high-frequency range (higher-order modes), as shown in Figure 2, the peak frequency for the optimized gear appears at 6512.50 Hz, a reduction of approximately 2270 Hz compared to the original design's 8782.50 Hz. This mode falls well outside the track's primary excitation band (1–5 kHz) and exhibits low amplitude; consequently, its engineering impact on the gear's fatigue life is negligible (as shown in Figure 27).

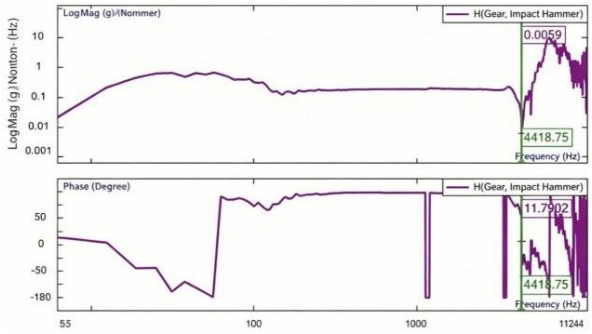


Figure 26 Optimized gear FRF magnitude and phase curves in the low-frequency range

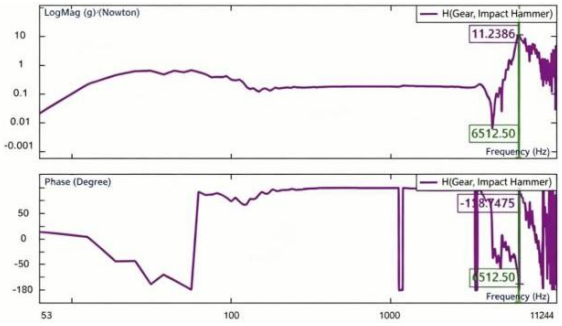


Figure27 Optimized FRF magnitude and phase curves of the gear in the high-frequency range

Comprehensive Evaluation: Table 4 compares key metrics between the original design and the optimized scheme (R = 1.5 mm). The optimized scheme simultaneously satisfies the dual objectives of static strength ($\sigma \leq 610.20$ MPa) and dynamic stability ($f \geq 4183$ Hz), with a curvature radius falling within the BOE range (1.32–1.60 mm) defined in Section 5.3; this validates the effectiveness of the PCI-BOE decision-making framework and the reliability of the engineering recommendation.

Table 4 Comparison of static and dynamic performance between the original design and the optimized scheme

Evaluation Metric	Original Design Value	Optimized Value （R=1.5 mm）	Change	Assessment
Maximum equivalent stress at tooth root (FEM)	688.95 MPa	601.45 MPa	↓ 12.7%	effectively alleviate
First-order bending modal frequency (EMA measured)	3637.5 Hz	4418.75 Hz	↑ 21.5%	Safe avoidance
Frequency-excitation margin	0% (within resonance zone)	21.5% （>15%）	Compliant	Resonance eliminated
BOE range compliance	Non-compliant	R=1.5∈[1.32, 1.60]	Compliant	Dual objectives met

The above validation results demonstrate that the failure-diagnosis-driven optimization strategy for variable-curvature splines has achieved the expected outcomes in both reducing tooth-root stress concentration and regulating natural frequencies, thereby providing an experimental basis for the fatigue-resistant design of differential gears for small all-terrain vehicles.

6 In conclusion

Focusing on the fracture failure of a small all-terrain vehicle (ATV) differential side gear, this study establishes a systematic design framework comprising "failure diagnosis, mechanism elucidation, structural optimization, and comprehensive verification." The main conclusions are as follows:

(1) Through finite element analysis and precise stress path zoning, the high-risk fracture zone was pinpointed to a local area defined by transverse coordinates [2.8, 4.2] mm and longitudinal coordinates [3, 5] mm at the gear root, providing a clear geometric target for subsequent optimization. Variable control analysis revealed the significant modulating effect of the stress orientation angle on peak stress, identifying 38° as the most critical loading angle.

(2) Metallographic analysis confirmed the failure mode as tooth surface spalling driven by overload impact; cross-verification indicated that the fracture resulted from stress concentration exceeding the material's strength limit under specific loading directions. Experimental modal analysis identified that the original design's first-order bending mode frequency (3637.5 Hz) fell within the track's primary excitation frequency band (1−5 kHz), posing a risk of resonance amplification.

(3) A variable-curvature gear root optimization scheme based on cubic B-splines achieved a continuous transition of the root fillet radius from 0.5 mm to 1.5 mm. Following optimization, the maximum equivalent stress at the gear root decreased from 688.95 MPa to 601.45 MPa (a 12.7% reduction), and the first-order bending mode frequency rose from 3637.5 Hz to 4418.75 Hz (a 21.5% increase), successfully avoiding the resonance-prone range defined by a 15% safety margin. Building on this, a joint decision-making framework integrating Physical Constraint Interpolation (PCI) and Bi-objective Optimization Envelope (BOE) was proposed. The PCI model was established as $\sigma(R) = 215.06 \cdot R^{-0.35} + 414.84$ MPa. By setting a 90% performance retention threshold for static strength and a 15% frequency safety margin for dynamic stability, a BOE range of $R \in [1.32, 1.60]$ mm was identified to satisfy both objectives, with a recommended engineering lower limit of $R \geq 1.40$ mm.

7 Funding

The project is supported by the Scientific Research Project of the Hebei Provincial Department of Education (No. BJ2026366).

8 Data Availability Declaration

All data generated and analyzed throughout this study are fully included within the manuscript. No supplementary or external data are available or required.

9 Reference

Behvar A, Tahmasbi K, Savich W, et al. Tooth interior fatigue fracture in automotive differential gears[J]. Engineering Failure Analysis, 2024, 156: 107829.

585 Ristić D. Numerical model for the critical stress determination in spur gears[J]. Sci. Tech. Rev., 2009
586 (1): 78-86.

587 Hwang S C, Lee J H, Lee D H, et al. Contact stress analysis for a pair of mating gears[J].
588 Mathematical and Computer Modelling, 2013, 57(1-2): 40-49.

589 Liu Y, Xu H, Dong C, et al. Analysis for meshing stiffness and transmission error of non-circular
590 gear based on finite element method[J]. Journal of Mechanical Science and Technology, 2025,
591 39(12): 7425-7435.

592 Guo Rensheng, Wei Xuanyan. Fundamentals of Mechanical Design [M]. Tsinghua University Press
593 Ltd., 2005.

594 Li Haifeng, Wu Jichuan, Liu Jianbo, et al. Finite Element Meshing and Mesh Quality Evaluation
595 Metrics [J]. China Mechanical Engineering, 2012, 23(3): 368-377.

596 Lü Zhonghe, Yang Jianwei. Finite Element Analysis and Experimental Study on Bending Fatigue of
597 Spur Gears in Subway Train Gearboxes [J]. Science Technology and Engineering, 2017, 17(8).

598 Fu Y, Zhuo Y, Zhou X, et al. Theoretical and experimental study on contact characteristics of spiral
599 bevel gears under quasi-static and large loading conditions[J]. Applied sciences, 2020, 10(15): 5109.

600 Zhang Y, Sun H, Liu B, et al. Surface crack analysis of the steering shaft gear after carburizing and
601 quenching[J]. Engineering Failure Analysis, 2022, 141: 106680.

602 Mbarek A, Del Rincon A F, Hammami A, et al. Comparison of experimental and operational modal
603 analysis on a back to back planetary gear[J]. Mechanism and Machine Theory, 2018, 124: 226-247.

604 Jiang Xingxing. Research on non-stationary vibration signal analysis and diagnosis method of key
605 components of gearbox [D]. Nanjing University of Aeronautics and Astronautics, 2016.

606 Yuan Y, Wang C, Vaidya K S, et al. Experimental and numerical studies on elastic vibrations of a
607 thin spinning gear with a novel tooth contact model[J]. Mechanical Systems and Signal Processing,
608 2025, 231: 112659.

609 Yang J, Zhang Y, Li R, et al. Temperature control-based design of variable damping and lightweight
610 gear bodies[J]. The International Journal of Advanced Manufacturing Technology, 2024, 131(3):
611 1807-1821.

612 Vaghela P, Prajapati J. Optimization of tooth root profile using bezier curve with G2 continuity to
613 reduce bending stress of asymmetric spur gear tooth[C]//MATEC Web of Conferences. EDP
614 Sciences, 2018, 237: 03010.

615 Chavadaki S, Kumar K C N, Rajesh M N. Finite element analysis of spur gear to find out the
616 optimum root radius[J]. Materials Today: Proceedings, 2021, 46: 10672-10675.

617 Spitas V, Costopoulos T, Spitas C. Increasing the strength of standard involute gear teeth with novel
618 circular root fillet design[J]. American Journal of Applied Sciences, 2005, 2(6): 1058-1064.

619 Kapelevich A L, Shekhtman Y V. Direct gear design: Bending stress minimization[J]. Gear
620 technology, 2003, 20(5): 44-47.

621 Dalcin R L, de Menezes V M, da Silva Rocha A, et al. Correlation between roughness, film thickness,
622 and friction coefficient with pitting wear resistance of spur gears[J]. The International Journal of
623 Advanced Manufacturing Technology, 2023, 129(11): 5473-5492.

624 Riera P, Vieira M, Rego R, et al. Efficient nonlinear spur gear analysis using an interpolated
625 analytical model[J]. Journal of the Brazilian Society of Mechanical Sciences and Engineering, 2026,
626 48(6): 437.

627 Zhu Y, Wang X, YafeiWang, et al. Robot trajectory planning for gear chamfer grinding based on
628 multi-objective collaborative optimization and quintic B-spline interpolation algorithm[J]. The
629 International Journal of Advanced Manufacturing Technology, 2025, 138(9): 4397-4414.